Mechanics, Electronics, Automation and Automatic Control
T. Xia (Ed.)
© 2024 The Authors.
This article is published online with Open Access by IOS Press and distributed under the terms of the Creative Commons Attribution Non-Commercial License 4.0 (CC BY-NC 4.0).
doi:10.3233/SAEM240038

Research on the Effect of Balance Parameters to the Force-Measurement System Output Result

Jinzhou LV[a], Canyu CAI[b], Qi WANG[a], Xiaoqing ZhANG[a,1], Zhengzhou LI[a], Jianxia LIU[a] and Yingchuan WU[a]
[a] *Aerospace Technology Institute, China Aerodynamics Research and Development Center, Mianyang, Sichuan, China, 621000*
[b] *School of Mechanical Engineering, Southwest Jiaotong University, Chengdu 610031, China*
ORCiD ID: Jinzhou LV https://orcid.org/0000-0001-6027-9451

Abstract. The measurement results of the force-measurement system (FMS) will be severely affected by the force balance when it is tested in the impulse combustion wind tunnels. To study this issue, the dynamics model of a 3-component FMS is established firstly. Then, 3 FMSs with different balance stiffness and 3 FMSs with different float frame stiffness are designed and the virtual calibration and modal analysis are carried out to acquire their stiffness matrices and modal parameters. Thirdly, the transient simulations of these 6 FMSs are conducted to obtain their responses. Finally, their measurement errors are analyzed before and after the inertia compensation. The mean measurement errors of these 6 FMSs are mostly lower than 0.2 % when the resonance vibration does not take place. This proves that the force balance parameters have a small influence on the mean measurement accuracy of the FMSs. In addition, the transient measurement errors show that F_x has a small relationship with the stiffness of the force balance, but F_y and M_z decrease with it. Meanwhile, the transient measurement errors also show that F_x decreases firstly, and then keeps remained with the stiffness of balance float frame, F_y keeps remained firstly, and then increases with it, and M_z keeps remained firstly, then decrease with it. Those research results will do much favor on the design of the impulse combustion wind tunnels force balance.

Keywords. Force-measurement system, balance, stiffness, inertia compensation, measurement error

1. Introduction

The ground facility is very important for the development of the hyper-sonic technology, which contains the long last tunnel, such as the 8-foot high temperature tunnel which was built in the Langley Research Center (LRC), and short last wind tunnel, such as the Φ 2.4 m impulse combustion wind tunnel which was built in the Chinese Aerodynamic Research and Development Center (CARDC). Because the test of a long last hyper-sonic wind tunnel is very expensive, the shock tunnel [1, 2] or the impulse wind tunnel [3 - 5]

[1] Corresponding Author: Xiaoqing ZHANG, 349313390@qq.com.

turn to be the most important facilities for the ground test. Since the test duration of them is very short, the excited vibration of the FMS in the startup period cannot be attenuated during the test. Therefore, the aerodynamic loads measurement technology become one of the key technologies in short duration wind tunnel test.

To solve the shock or impulse wind tunnel aerodynamic loads measurement problem, many scholars have done research works. Tanno [6 - 8], Singh [9, 10], Sahoo [11], Trivedi [12], Satheesh [13], Saravanan [14,15], and Naumann [16] used an accelerometer balance to measure the aerodynamic loads in a shock tunnel. Meanwhile, the stress-wave balance [17, 18], optical balance technique [19, 20, 21], strain balance technique [22, 23], and piezoelectric balance [24] were also applied in the past. For example, Marineau [25] built up a piezoelectric balance, and in his test the outputs were compensated with acceleration. Watari [26] proposed an oscillation identification method to extract aerodynamic load or moment from oscillation contaminated short duration measurement data. Li [27, 28] used artificial intelligence technology to intelligently identify aerodynamic forces without relying on expert prior knowledge and achieved good results.

In summary, most test in above researches were carried out in a shock tunnel whose test duration is less than 10 milliseconds. But the test time of many wind tunnels built nowadays in China could be longer than 100 ms, such as the Φ 2.4 m impulse combustion wind tunnel and JF-12 [29, 30] shock tunnel. To acquire the aerodynamic loads of the test model, the force balance of the FMS should have a high stiffness to reduce the influence of fluid-structure coupling effect on the model attitude. Therefore, the foil strain-gauge balance turned to be a priority choice for an impulse wind tunnel force measurement. Wang [29, 30] has conducted an aerodynamic loads measurement test through this kind of balance in JF-12 shock tunnel. Lv [31, 32] deduced the dynamics equation of the FMS and verified the inertia compensation method both through the finite element method (FEM) and wind tunnel test. But the effect of the force balance parameters to the FMS output are not studied. Therefore, 6 FMSs with different element stiffness and float frame stiffness are designed, firstly. Secondly, the static virtual calibration, modal analysis, transient simulation of them are conducted through the FEM. Thirdly, the measurement error analysis of above simulation outputs both before and after the inertia compensation method are calculated. Finally, the effect of the force balance stiffness and the float frame stiffness of the force balance to the output of the FMS are acquired.

2. Description of the FMS

The impulse combustion wind tunnel FMS is shown in Figure 1, which is mainly consisted of test model, force balance, and pedestal. The test model in this figure is simplified to reduce its complexity of the research.

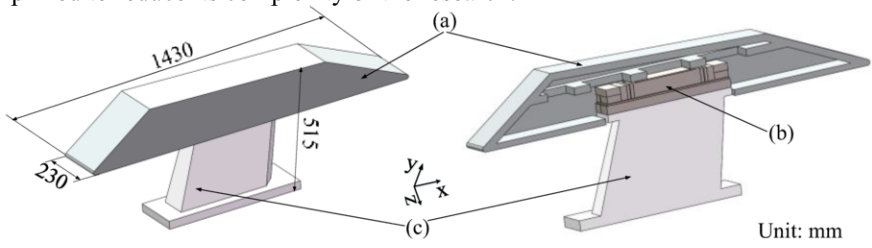

Figure 1. FMS, (a) test model, (b) force balance, (c) pedestal.

The force balance is shown in Figure 2 and Figure 3, which consisted of a float frame, a fix frame, some measurement elements, and some support elements. Figure 2 shows the balance *a*, *b*, and *c* with different measurement elements and support beams. The thicknesses of the F_x measurement elements *l* are 3.6 mm, 4.3 mm, and 5mm, respectively. The thicknesses of the F_y and M_z measurement elements *m* are 5 mm, 7.1 mm, and 9.2 mm, respectively. And the thicknesses of the support elements *n* are 1.5 mm, 1.85 mm, and 2.2 mm, respectively. In a word, the stiffness of force balances *a*, *b*, and *c* is increased gradually in each component. For the convenience of description, the FMS with force balance *a*, *b*, and *c* are noted by FMS-A, FMS-B and FMS-C.

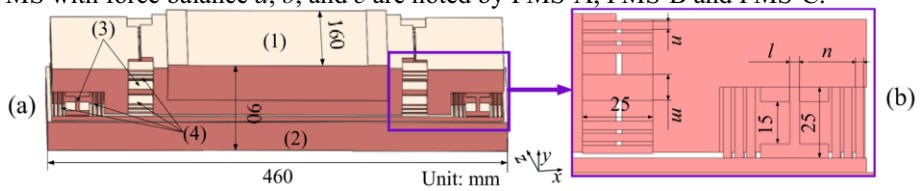

Figure 2. Force balance *a*, *b*, and *c* (1) float frame, (2) fix frame, (3) measurement elements, and (4) support beams.

Figure 3 shows the force balance *d*, *e*, and *f* with different float frame stiffness. The float frame thickness *h* of the force balance *d*, *e*, and *f* are 49 mm, 75mm, and 100 mm. And the thickness of the measurement elements and support beams are all the same as shown in Figure 3 (a). The FMS with force balance *d*, *e*, and *f* are noted by FMS-D, FMS-E and FMS-F.

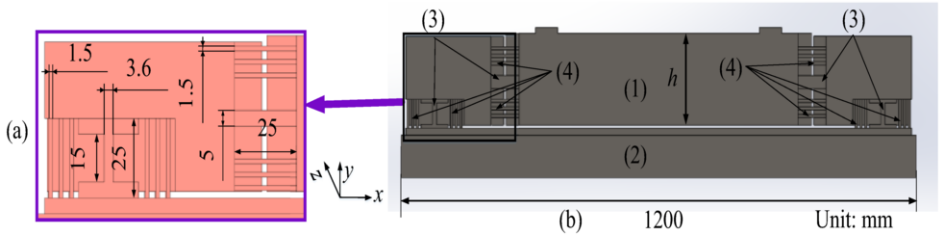

Figure 3. Force balances *d*, *e*, and *f*, (1) float frame, (2) fix frame, (3) measurement elements, and (4) support beams.

3. Dynamic model of the FMS

The simplified FMS is shown in Figure 4 (a). The pedestal and the fix frame of the force balance are simplified as a rigid body, the test model and the float frame are treated as a whole. The largest strain occurred on the measurement elements during the test. Therefore, the FMS could be further simplified into a beam-spring-damping system as shown in Figure 4 (b). In this figure, the measurement elements of the force balance are modeled as 4 springs k_1 - k_4. Considering the symmetry of the force balance, the stiffness k_1 is equal to k_2, k_3 is equal to k_4, respectively. The damping of the FMS is modeled as c_1 - c_4. Finally, the dynamic equation of the FMS is deduced based on the Figure 4 (b) as follows:

$$\boldsymbol{M}\ddot{\boldsymbol{q}} + \boldsymbol{C}\dot{\boldsymbol{q}} + \boldsymbol{K}\boldsymbol{q} = \boldsymbol{F} \tag{1}$$

where, $\boldsymbol{M}$, $\boldsymbol{C}$, and $\boldsymbol{K}$ are the global mass, damping, and stiffness matrix, $\boldsymbol{q}$ and $\boldsymbol{F}$ are the vector of nodal displacement and aerodynamic loads, respectively. For the FMS of the impulse combustion wind tunnel, its vibration is mainly governed by the system

parameters $\boldsymbol{M}$ and $\boldsymbol{K}$, because the damping matrix $\boldsymbol{C}$ is quite small and ignored in this paper, and this method was verified in the reference [31, 32].

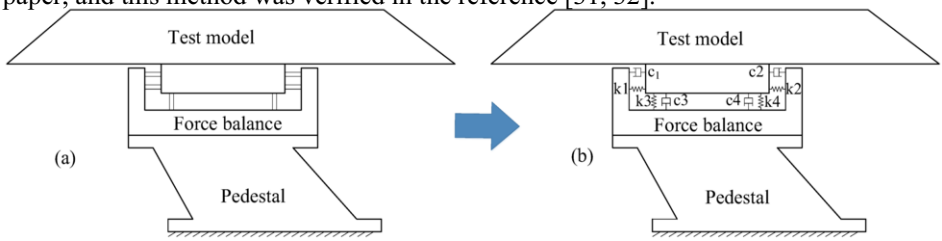

Figure 4. Simplification of the FMS.

Virtual calibration of these FMSs is conducted in this section to calculate their stiffness matrix $\boldsymbol{K}$. The positions of the strain gauge on the force balance are shown in Figure 5, which approach the root of the measurement elements. Where, the points X1 - X8 are used to measure the drag force F_x, which output the y-direction strains, and noted as μ_{X1} - μ_{X8}, respectively. The points Y1 - Y8 are used to measure the lift force F_y, which output the x-directions strains, and noted as μ_{Y1} - μ_{Y8}, respectively. The points M1 - M8 are used to measure the pitching moment M_z, which output the x-direction strains, too, and noted as μ_{M1} - μ_{M8}, respectively.

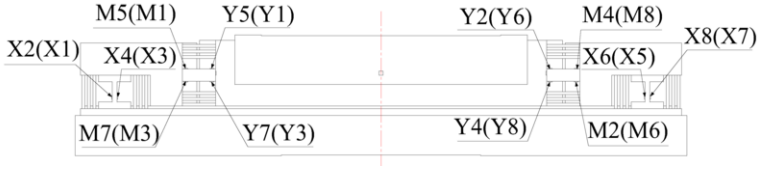

Figure 5. Strain gauge positions of the 3-component force balance.

The static formula of the FMS is presented as follows:

$$\boldsymbol{F} = \boldsymbol{U}\boldsymbol{K} \tag{2}$$

Where, $\boldsymbol{F} = \begin{pmatrix} F_x \\ F_y \\ M_z \end{pmatrix}$, $\boldsymbol{U} = \frac{2}{4}\times 10^6 \times \begin{pmatrix} \mu_{X1}+\mu_{X2}-\mu_{X3}-\mu_{X4}+\mu_{X5}+\mu_{X6}-\mu_{X7}-\mu_{X8} \\ \mu_{Y1}+\mu_{Y2}-\mu_{Y3}-\mu_{Y4}+\mu_{Y5}+\mu_{Y6}-\mu_{Y7}-\mu_{Y8} \\ \mu_{M1}+\mu_{M2}-\mu_{M3}-\mu_{M4}+\mu_{M5}+\mu_{M6}-\mu_{M7}-\mu_{M8} \end{pmatrix}$,

$\boldsymbol{K} = \begin{pmatrix} k_{11} & k_{12} & k_{13} \\ k_{21} & k_{22} & k_{23} \\ k_{31} & k_{32} & k_{33} \end{pmatrix}$.

In the vector $\boldsymbol{F}$, F_x, F_y, and M_z are the drag force, lift force, and pitching moment, respectively. In the matrix $\boldsymbol{K}$, k_{11}, k_{22}, and k_{33} are the principal coefficients, k_{12}, k_{13}, k_{21}, k_{23}, k_{31}, and k_{32} are the interference coefficients.

Then, the coefficient matrix can be derived through matrix transform.

$$\boldsymbol{K} = \boldsymbol{U}^{-1}\boldsymbol{F} \tag{3}$$

To acquire the coefficient $\boldsymbol{K}$, it is necessary to apply 3 uncorrelated loads on the FMS and acquire the force balance output strains correspondingly. Then, the coefficient matrix can be calculated.

3.1. Virtual calibration of the FMSs

3.1.1. Virtual calibration of the FMS-A, FMS-B, and FMS-C

The finite element models of FMS-A, FMS-B, and FMS-C are shown in Figure 6. The mesh of FMS-A embraces 179,859 nodes and 32,112 elements, the FMS-B embraces 137,833 nodes and 23,192 elements, and the FMS-C embraces 237,422 nodes and 46,085 elements, respectively. They are all meshed with a hexahedral element. The grid size of the measurement and support elements which would bear large strains are refined as shown in Figure 6 (b). In addition, to verify the mesh independence, they are refine meshed as shown in Figure 6 (c) and (d). The refined mesh of FMS-A embraces 584,323 nodes and 124,241 elements. The FMS-B embraces 580,262 nodes and 123,386 elements. And the FMS-C embraces 628,710 nodes and 131,766 elements. The test model and the pedestal are made of structural steel, whose density is 7,850 kg/m^3, Young's Modulus is 200 GPa, and Poisson's Ratio is 0.3. Meanwhile, the material of the force balance is 00Ni18Co8Mo5TiAl whose density is 8,000 kg/m^3, Young's Modulus is 187.25 GPa, and Poisson's Ratio is 0.27. The bottom of the pedestal is fixed during the simulation which is consistent with the wind tunnel test. During the calibration, the input loads are $\mathbf{F}_1 = (-2{,}000, 0, 0)^T$, $\mathbf{F}_2 = (0, 3{,}000, 0)^T$, and $\mathbf{F}_3 = (0, 0, 1{,}000)^T$, whose units are N or Nm. The loading position is the surface of the test model, as shown in Figure 6 (a) and (c).

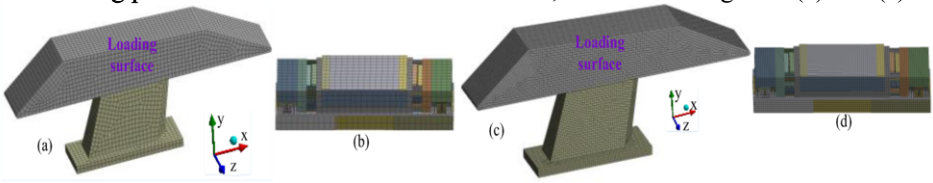

Figure 6. Finite element models of the FMS-A, FMS-B, and FMS-C (a), balance (b), refinement models of the FMS-A, FMS-B, and FMS-C (c), refinement balance (d).

As for the FMS-A, the coefficient matrix calculated through equation (3) before and after the mesh refinement are as follows:

$$\boldsymbol{K}_{A1} = \begin{pmatrix} 1.0152 & -8.9\times10^{-5} & -5.6\times10^{-2} \\ -6.4\times10^{-5} & 2.5156 & 2.2\times10^{-4} \\ -1.3\times10^{-3} & 1.4\times10^{-4} & 0.5046 \end{pmatrix},$$

$$\boldsymbol{K}_{A2} = \begin{pmatrix} 1.0087 & -6.6\times10^{-5} & -0.05606 \\ -3.1\times10^{-5} & 2.48853 & 1.6\times10^{-4} \\ 6.4\times10^{-4} & 1.4\times10^{-4} & 0.49896 \end{pmatrix}.$$

As for the FMS-B, the coefficient matrix calculated through equation (3) before and after the mesh refinement are as follows:

$$\boldsymbol{K}_{B1} = \begin{pmatrix} 1.6444 & 6.5\times10^{-4} & -6.1\times10^{-3} \\ 4.4\times10^{-4} & 6.0726 & 0.1822 \\ -2.1\times10^{-2} & 1.6\times10^{-3} & 1.1698 \end{pmatrix}, \quad \boldsymbol{K}_{B2} = \begin{pmatrix} 1.6434 & 3.7\times10^{-4} & 6.4\times10^{-3} \\ -2.8\times10^{-4} & 6.039 & 3.5\times10^{-2} \\ 1.2\times10^{-2} & 4.0\times10^{-4} & 1.137 \end{pmatrix}.$$

As for the FMS-C, the coefficient matrix calculated through equation (3) before and after the mesh refinement are as follows:

$$\boldsymbol{K}_{C1}=\begin{pmatrix} 2.12096 & -9.7\times10^{-4} & -9.51\times10^{-3} \\ 4.2\times10^{-5} & 9.71962 & -5.99\times10^{-2} \\ -6.8\times10^{-2} & 4.6\times10^{-3} & 2.0998 \end{pmatrix},$$

$$\boldsymbol{K}_{C2}=\begin{pmatrix} 2.1248 & -8.4\times10^{-4} & -9.4\times10^{-3} \\ -3.8\times10^{-5} & 9.6911 & -5.9\times10^{-2} \\ -7.0\times10^{-2} & 4.6\times10^{-3} & 2.11305 \end{pmatrix}.$$

As the stiffness matrixes $\boldsymbol{K}_{A1}$ and $\boldsymbol{K}_{A2}$, $\boldsymbol{K}_{B1}$ and $\boldsymbol{K}_{B2}$, $\boldsymbol{K}_{C1}$ and $\boldsymbol{K}_{C2}$ show that the principal coefficient deviation ratios are less than 1.1 %, 2.8 %, and 0.63% before and after the mesh refinement. And the mesh dependence of FMSs is verified. Meanwhile, this indicates that the finite element models of the FMSs before the refinement could meet the precision requirement, and $\boldsymbol{K}_{A1}$, $\boldsymbol{K}_{B1}$, and $\boldsymbol{K}_{C1}$ could be treated as the stiffness matrix of FMS-A, FMS-B, and FMS-C, respectively. In addition, the absolute values of the principal coefficients of $\boldsymbol{K}_{A1}$, $\boldsymbol{K}_{B1}$, and $\boldsymbol{K}_{C1}$ are increased gradually, which illustrate that the stiffness of the FMS-A, FMS-B, and FMS-C are increased gradually.

3.2. Virtual calibration of the FMS-D, FMS-E, and FMS-F

As to the FMS-D, FMS-E, and FMS-F, the finite element model and the refinement model are shown in Figure 7. The mesh of FMS-D contains 118,541 nodes and 19,104 elements, FMS-E contains 122,144 nodes and 19,872 elements, and FMS-F contains 129,350 nodes and 21,408 elements. The refinement model of FMS-D contains 1,893,053 nodes and 419,797 elements, the FMS-E contains 1,930,007 nodes and 428,379 elements, and the FMS-F contains 1,966,709 nodes and 436,717 elements. Meanwhile, the materials of each component and the boundary condition of the FMS-D, FMS-E, FMS-F are the same with the FMS-A, FMS-B, and FMS-C.

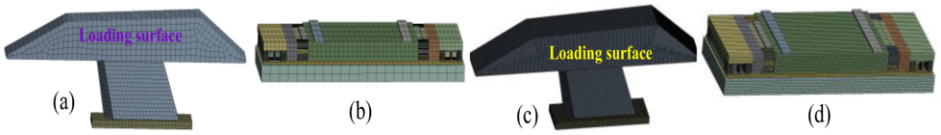

Figure 7. Finite element models of the FMS-D, FMS-E, and FMS-F (a), balance (b), refinement models of the FMS-D, FMS-E, and FMS-F (c), balance (d).

As for the FMS-D, the coefficient matrix calculated through equation (3) before and after the mesh refinement are as follows:

$$\boldsymbol{K}_{D1}=\begin{pmatrix} -2.2216 & 4.49\times10^{-4} & 6.63\times10^{-3} \\ -5.55\times10^{-5} & 7.6938 & -7.42\times10^{-3} \\ 0.1511 & -5.71\times10^{-3} & -1.5559 \end{pmatrix},$$

$$\boldsymbol{K}_{D2}=\begin{pmatrix} -2.2032 & 8.09\times10^{-4} & 6.11\times10^{-3} \\ -2.89\times10^{-5} & 7.5463 & 3.69\times10^{-4} \\ 0.1295 & -5.83\times10^{-3} & -1.5168 \end{pmatrix}.$$

As for the FMS-E, the coefficient matrix calculated through equation (3) before and after the mesh refinement are as follows:

$$\boldsymbol{K}_{\mathrm{E1}}=\begin{pmatrix} -2.2129 & 2.61\times10^{-4} & -1.49\times10^{-2} \\ 5.18\times10^{-5} & 7.6882 & -8.57\times10^{-4} \\ 4.57\times10^{-2} & -5.20\times10^{-4} & -1.6729 \end{pmatrix},$$

$$\boldsymbol{K}_{\mathrm{E2}}=\begin{pmatrix} -2.1435 & 9.48\times10^{-4} & -1.53\times10^{-2} \\ -4.52\times10^{-4} & 7.7700 & -6.72\times10^{-4} \\ 3.63\times10^{-2} & -3.27\times10^{-3} & -1.6382 \end{pmatrix}.$$

As for the FMS-F, the coefficient matrix calculated through equation (3) before and after the mesh refinement are as follows:

$$\boldsymbol{K}_{\mathrm{F1}}=\begin{pmatrix} -2.3666 & 5.65\times10^{-4} & -3.91\times10^{-2} \\ 1.48\times10^{-4} & 8.1894 & -8.07\times10^{-4} \\ 3.10\times10^{-2} & -3.33\times10^{-3} & -1.7277 \end{pmatrix},$$

$$\boldsymbol{K}_{\mathrm{F2}}=\begin{pmatrix} -2.3118 & 7.43\times10^{-4} & -3.92\times10^{-2} \\ 1.70\times10^{-4} & 8.1917 & -8.12\times10^{-4} \\ 2.37\times10^{-2} & 3.18\times10^{-3} & -1.7247 \end{pmatrix}.$$

Comparing $\boldsymbol{K}_{\mathrm{D1}}$ and $\boldsymbol{K}_{\mathrm{D2}}$, $\boldsymbol{K}_{\mathrm{E1}}$ and $\boldsymbol{K}_{\mathrm{E2}}$, $\boldsymbol{K}_{\mathrm{F1}}$ and $\boldsymbol{K}_{\mathrm{F2}}$, we can find that the principal coefficient deviation ratios are less than 2.6 %, 3.2 %, and 2.4%, respectively, which proves that the stiffness of the FMS-D, FMS-E, and FMS-F is close to each other. Meanwhile, the finite element model before refinement could meet the precision requirement of this research.

3.3. Extraction of the inertia load

It is very difficult to obtain the exact inertia loads of the FMS because the float frame of the force balance and the test model would bear flexible deformations more or less during the test. Figure 8 shows the modal analysis result of the FMSs and the oscillation mode of its force balance. Figure 8 (a) is the third order or F_{x}-direction mode which is the oscillation of the test model, float frame, and connection parts of the float and fix frame. Figure 8 (b) and (c) are the fifth or F_{y}-direction mode and first or M_{z}-direction mode which are mainly oscillation of the float frame and the test model. Through the method of reference [31, 32], the global mass matrices $\boldsymbol{M}$ of the FMS-A, FMS-B, and FMS-C are calculated through the 3-D design software as follows:

$$\boldsymbol{M}_{\mathrm{A}}=\boldsymbol{M}_{\mathrm{B}}=\boldsymbol{M}_{\mathrm{C}}=\begin{pmatrix} m_x & & \\ & m_y & \\ & & J_z \end{pmatrix}=\begin{pmatrix} 210.364 & & \\ & 201.861 & \\ & & 28.536 \end{pmatrix}.$$

And the global mass matrices $\boldsymbol{M}$ of the FMS-D, FMS-E, and FMS-F are as follows:

$$\boldsymbol{M}_{\mathrm{D}}=\begin{pmatrix} 194.3 & & \\ & 200.41 & \\ & & 27.86 \end{pmatrix},\ \boldsymbol{M}_{\mathrm{E}}=\begin{pmatrix} 199.23 & & \\ & 208.33 & \\ & & 27.90 \end{pmatrix},$$

$$\boldsymbol{M}_{\mathrm{F}}=\begin{pmatrix} 204.17 & & \\ & 216.38 & \\ & & 27.97 \end{pmatrix}.$$

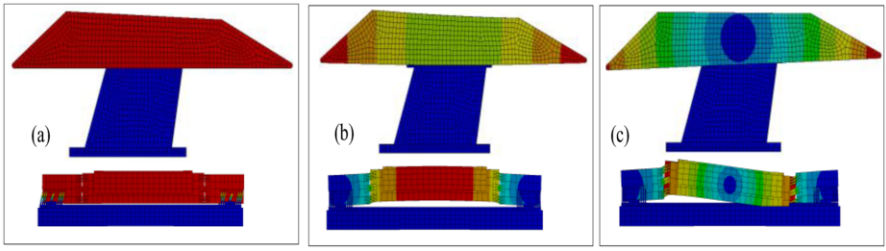

Figure 8. Mode shapes (a) F_x-direction mode, (b) F_y-direction mode, and (c) M_z-direction mode.

In above matrices, m_x is the mass in x-direction vibration, m_y is the mass in y-direction vibration, and J_z is the moment of inertia around z-axis.

In order to acquire the inertia loads as exact as possible, 10 acceleration points are taken into consideration. Figure 9 shows the acceleration detection points, A1 - A6 are the points on the force balance and A7 - A10 are the points on the test model. Finally, the acceleration $\boldsymbol{A}$ of the FMSs is presented as follows:

$$\boldsymbol{A}=\begin{pmatrix} a_x \\ a_y \\ \alpha_{M_z} \end{pmatrix}=\begin{pmatrix} \frac{1}{10}(A1_x+A2_x+\cdots+A10_x) \\ \frac{1}{10}(A1_y+A2_y+\cdots+A10_y) \\ \frac{1}{4\times 0.708}(A7_y+A8_y+A9_y+A10_y) \end{pmatrix} \tag{4}$$

Finally, the inertia loads acquired through the Newton's second law are as follows:

$$\boldsymbol{F}_I=\boldsymbol{MA} \tag{5}$$

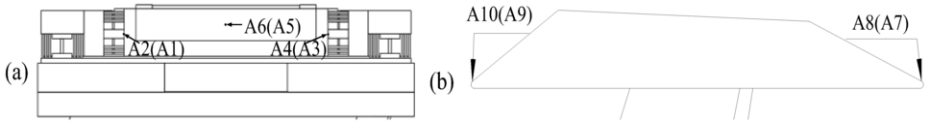

Figure 9. Acceleration detection points, (a) points on the force balance, (b) points on the test model.

4. Input loads of the FMS

The test result of an FMS during the impulse wind tunnel test is shown in Figure 10. As illustrated in this figure, the T-pressure of the test chamber climbs up in a short period (about 300 - 350 ms) after the wind tunnel startup, then, achieves an approximate stable level about 580 - 1040 ms. The airflow exerts on the surface of the test model. It is just the shock loads that excite the vibration of the FMS. Therefore, it is necessary to apply a shock loads on the FMS to study its transient output.

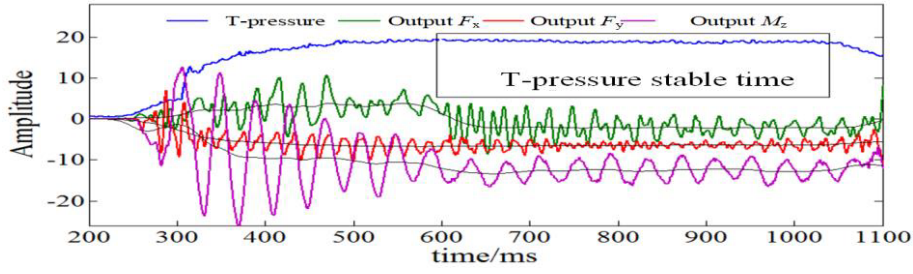

Figure 10. Variations of the total pressure and force balance output in the impulse wind tunnel test.

Meanwhile, it is seen in this figure that all the output loads of the force balance are approximate to the sine loads. According to the loads changing history of the FMS, the sine loads are another input form. To determine the input frequency of the sine loads, modal analysis of the FMS is conducted. The results are shown in Figure 8 and Table 1. Because the purely single component force or moment does not exist during the test, the input loads of the FMS are 3-component simultaneously. In order to study the effect of the force balance parameters to the aerodynamic load measurement, the frequencies of the input loads are lower and higher than the natural frequency of FMS-A, FMS-B, and FMS-C which are noted as sine loads A and B, respectively. Similarly, we define the sine loads C and D, whose frequencies are lower and higher than the natural frequencies of FMS-D, FMS-E, and FMS-F. The amplitudes, frequencies, and loading time of the input loads are shown in Table 2.

Table 1. Mode parameters of the FMSs.

FMS-A		FMS-B		FMS-C		FMS-D		FMS-E		FMS-F		Mode description
Order	*f*/Hz	Order	*f*/Hz	Order	*f*/Hz	Order	*f*/Hz	Order	*f*/Hz	Order	*f*/Hz	
3	97.7	3	73.0	3	121.0	3	150.2	3	145.2	3	148.3	F_x-direction
5	115.3	6	109.0	6	172.6	5	159.8	5	173.3	5	185.3	F_y-direction
1	55.6	1	156.2	1	80.6	1	69.8	1	80.1	1	87.7	M_z-direction

Table 2. Parameters of the input forces and moment.

Loads	F_x		F_y		M_z		Loading time (ms)		
	Amplitude/N	*f*/Hz	Amplitude/N	*f*/Hz	Amplitude/Nm	*f*/Hz	0	Sine loads	0
A	2,000	60	3,000	80	1,000	30	0 - 21	21 - 170	170 - 250
B	2,000	160	3,000	200	1,000	110	0 - 21	21 - 170	170 - 250
C	2,000	100	3,000	100	1,000	50	0 - 10	10 - 190	190 - 250
D	2,000	250	3,000	200	1,000	120	0 - 10	10 - 80	80 - 120

5. Simulation result

5.1. Simulation results of the FMS-A, FMS-B, and FMS-C

5.1.1. Simulation result of the FMS-A, FMS-B, and FMS-C under the action of the shock loads

The analysis results of FMS-A, FMS-B and FMS-C under the action of the shock loads are illustrated in Figure 11. Figure 11 (a) shows the input forces and moment. The results of the FMS-A, FMS-B, and FMS-C after the inertia compensation are shown in Figure 11 (b), (c), (d), respectively. From these figures we know that the oscillations of the outputs are approximately suppressed after the inertia compensation. The outputs and inputs are nearly consistent with each other. As for the FMS-A, the output amplitudes of F_x, F_y, and M_z are are -2,051.0 N, 3,117.1 N, and 1,160.7 Nm, respectively. As for the FMS-B, the output amplitudes of F_x, F_y, and M_z are -2,048.89 N, 3,200.47 N, and 1,031.32 Nm, respectively. As for the FMS-C, the output amplitudes of F_x, F_y, and M_z are -2,083.5 N, 3,198.2 N, and 1,050.6 Nm, respectively.

5.1.2. Simulation result of the FMS-A, FMS-B, and FMS-C under the action of the sine loads A

The analysis results of FMS-A, FMS-B, and FMS-C under the action of the sine loads A are illustrated in Figure 12. Figure 12 (a) shows the input forces and moment. Figure 12 (b), (c), and (d) show their analysis results after the inertia compensation. As for the FMS-A, the output amplitudes of F_x, F_y, and M_z are 2,055.5 N, 3,031.3 N, and 1,009.1 Nm, respectively. As to the FMS-B, the output amplitudes of F_x, F_y, and M_z are 2,067.2 N, 3,014.1 N, and 1,097.4 Nm, respectively. As to the FMS-C, the output amplitudes of F_x, F_y, and M_z are 2,055.5 N, 3,031.3 N, and 1,009.1 Nm, respectively. From these figures we can see that the FMSs vibrate in a coupling form of a free and forced form when the sine loads A is applied on them. Their output histories are approximately consistent with the inputs after the inertia compensation.

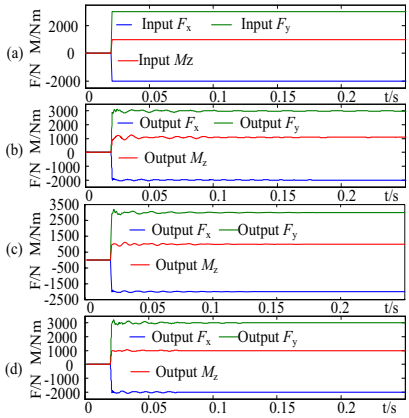

Figure 11. Transient simulation result of the FMS-A, FMS-B, and FMS-C under the action of the shock loads, (a) the input loads, (b) output of the FMS-A, (c) output of the FMS-B, (d) output of the FMS-C.

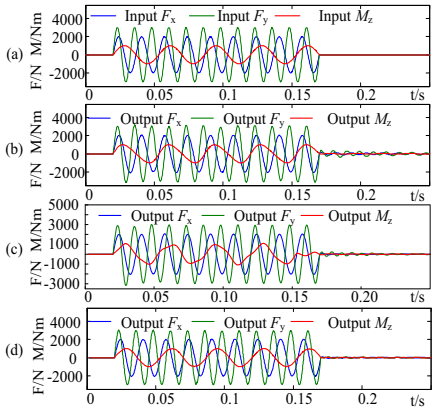

Figure 12. Transient simulation result of the FMS-A, FMS-B, and FMS-C under the action of sine loads A, (a) the input loads, (b) output of the FMS-A, (c) output of the FMS-B, (d) output of the FMS-C.

5.1.3. Simulation result of the FMS-A, FMS-B, and FMS-C under the action of the sine loads B

FMS-A, FMS-B, and FMS-C under the action of sine loads B is illustrated in Figure 13 (b), (c), and (d). As for the FMS-A, the output amplitudes of F_x, F_y, and M_z are 1,973.9 N, 2,949.9 N, and 1,181.1 Nm after the inertia compensation, respectively. As for the FMS-B, the output amplitudes of F_x, F_y, and M_z are -2,082.2 N, 3,257.9 N, and -1,257.2 Nm after the inertia compensation, respectively. As for the FMS-C, the output amplitudes of F_x, F_y, and M_z are 1,929.2 N, 3,399.9 N, and 1,108.3 Nm after the inertia compensation, respectively. From these figures we can see that the FMSs are vibrating in the coupling form of free and forced vibration when the sine loads B is applied on them. The outputs are approximately consistent with the input after the inertia compensation.

5.2. Simulation results of the FMS-D, FMS-E, and FMS-F

5.2.1. Simulation result of the FMS-D, FMS-E, and FMS-F under the action of the shock loads

The analysis results of FMS-D, FMS-E, and FMS-F under the action of the shock loads are illustrated in Figure 14. Figure 14 (a) shows the input forces and moment. Figure 14 (b), (c), and (d) shows their analysis results after the inertia compensation. As to the FMS-D, the output amplitudes of F_x, F_y, and M_z are -2,103.64 N, 3,123.02 N, and 1,038.54 Nm, respectively. As to the FMS-E, the output amplitudes of F_x, F_y, and M_z are -2,075.00 N, 3,110.72 N, and 1,0446.67 Nm, respectively. As to the FMS-F, the output amplitudes of F_x, F_y, and M_z are -2,117.14 N, 3,123.88 N, and 1,058.95 Nm, respectively.

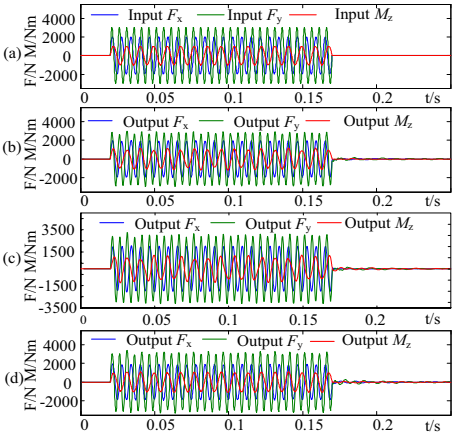

Figure 13. Transient simulation result of the FMS-A, FMS-B, and FMS-C under the action of sine loads B, (a) the input loads, (b) output of the FMS-A, (c) output of the FMS-B, (d) output of the FMS-C.

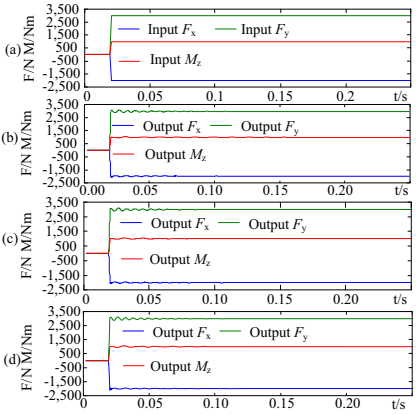

Figure 14. Transient simulation result of the FMS-D, FMS-E, and FMS-F under the action of shock loads, (a) input loads, (b) output of the FMS-D, (c) output of the FMS-E, (d) output of the FMS-F.

5.2.2. Simulation result of the FMS-D, FMS-E, and FMS-F under the action of the sine loads C

The analysis results of FMS-D, FMS-E, and FMS-F under the action of the sine loads C are illustrated in Figure 15. Figure 15 (a) shows the input forces and moment. Figure 15 (b), (c), and (d) shows their analysis results after the inertia compensation. As to the FMS-D, the output amplitudes of F_x, F_y, and M_z are -1,997.94 N, -2,959.97 N, and 1,002.4 Nm, respectively. As to the FMS-E, the output amplitudes of F_x, F_y, and M_z are -2,047.61 N, 3,046.46 N, and 984.32 Nm, respectively. As to the FMS-F, the output amplitudes of F_x, F_y, and M_z are -2,057.52 N, 3,050.85 N, and -1,014.34 Nm, respectively. From these figures we can see that the FMSs vibrate in the coupling form of a free and forced form when the sine loads C is applied on them. Their output histories are approximately consistent with the inputs after the inertia compensation.

5.2.3. Simulation result of the FMS-D, FMS-E, and FMS-F under the action of the sine loads D

The analysis results of FMS-D, FMS-E and FMS-F under the action of the sine loads D are illustrated in Figure 16. Figure 16 (a) shows the input forces and moment. Figure 16 (b), (c), and (d) shows their analysis results after the inertia compensation. As to the FMS-D, the output amplitudes of F_x, F_y, and M_z are -2,045.78 N, 2,896.43 N, and -1,084.78 Nm, respectively. As to the FMS-E, the output amplitudes of F_x, F_y, and M_z are -1996.5 N, 2,976.28 N, and -1,014.79 Nm, respectively. As to the FMS-F, the output amplitudes of F_x, F_y, and M_z are 2,007.75 N, -2,991.04 N, and -1,007.91 Nm, respectively. From these figures we can see that the FMSs vibrate in the coupling form of a free and forced form when the sine loads F is applied on them. Their output histories are approximately consistent with the inputs after the inertia compensation.

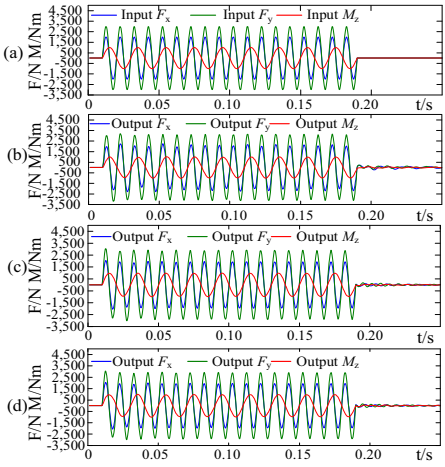

Figure 15. Transient simulation result of the FMS-D, FMS-E, and FMS-F under the action of sine loads C, (a) input loads, (b) output of the FMS-D, (c) output of the FMS-E, (d) output of the FMS-F.

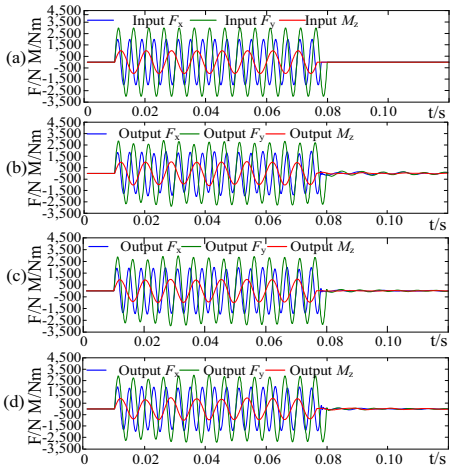

Figure 16. Transient simulation result of the FMS-D, FMS-E, and FMS-F under the action of sine loads D, (a) input loads, (b) output of the FMS-D, (c) output of the FMS-E, (d) output of the FMS-F.

6. Measurement error analysis of the FMS

In this paper, the measurement error rate is defined the same as paper [31, 32]:

$$\alpha = |E| / A . \tag{6}$$

where E is the measurement error of the FMS, and A is the amplitude of the input loads during the analysis.

6.1. Measurement error analysis of the FMS-A, FMS-B, and FMS-C

6.1.1. Mean measurement error analysis of the FMS-A, FMS-B, and FMS-C

The mean measurement error rates of the FMS-A, FMS-B, and FMS-C after the inertia compensation in F_x, F_y, and M_z component are shown in Table 3. From this table, we know that the mean measurement error rates of the FMSs are mostly lower than 0.15 %

when the shock loads are applied, lower than 0.2 % when the sine loads A are applied, and lower than 0.1 % when the sine loads B are applied. This result indicates that it is feasible to treat the mean elastic output after the inertia compensation as the static aerodynamic loads. In addition, the mean measurement errors have a small change after the inertia compensation by comparing the output results of them under the same loading. This proves that the stiffness of the force balance has a little influence on the mean measurement errors of the FMS.

Table 3. Mean measurement error rates of the FMS-A, FMS-B, and FMS-C after the inertia compensation.

Loads	FMS-A			FMS-B			FMS-C		
	F_x (‰)	F_y (‰)	M_z (‰)	F_x (‰)	F_y (‰)	M_z (‰)	F_x (‰)	F_y (‰)	M_z (‰)
Shock loads	0.20	0.29	0.13	1.42	0.73	0.15	0.04	0.7	0.80
Sine loads A	0.45	1.52	1.44	0.23	0.89	1.93	0.41	0.24	0.10
Sine loads C	0.29	0.67	0.67	0.35	0.25	3.33	0.59	0.11	0.72

6.1.2. Transient measurement error rate analysis of the FMS-A, FMS-B, and FMS-C

The transient measurement errors of these three FMSs after the inertia compensation are shown in Figure 17. Figure 17 (a) - (c) are the measurement errors of the FMS-A in F_x, F_y, and M_z component, and (d) - (f) are the measurement errors of the FMS-B, and (g) - (i) are the measurement errors of the FMS-C.

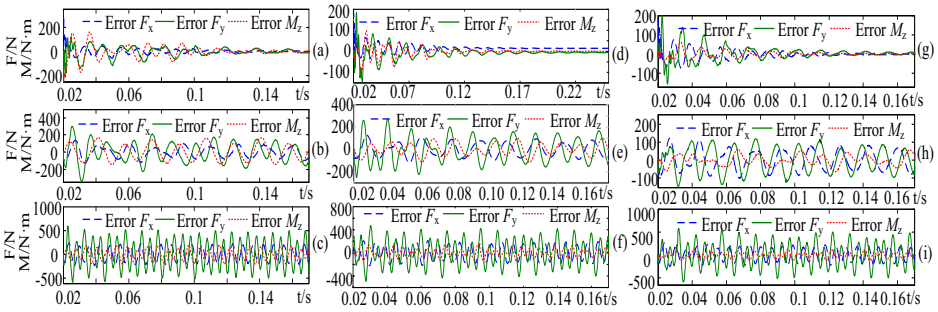

Figure 17. The transient measurement errors of FMSs, (a) - (c) the errors of FMS-A, (d) - (f) the errors of FMS-B, (g) - (i) the errors of FMS-C.

Table 4 shows the maximum transient measurement error rates of the FMS-A, FMS-B, and FMS-C. We can find in this table that the transient output histories of the FMSs are close to the input loads. Meanwhile, the measurement error rate of F_x change a little with the stiffness of the force balance, but the measurement error rates of F_y and M_z decrease with the increase of the force balance stiffness.

Table 4. The maximum measurement error rates of the FMS-A, FMS-B, and FMS-C after the inertia compensation.

Load	FMS-A (%)			FMS-B (%)			FMS-C (%)		
	Shock loads	Loads A	Loads B	Shock loads	Loads A	Loads B	Shock loads	Loads A	Loads B
F_x	2.75	6.24	11.28	3.24	6.36	11.18	3.24	6.05	9.07
F_y	4.71	11.27	19.86	3.33	9.00	16.52	2.96	4.85	10.95
M_z	13.93	15.83	19.72	9.84	11.55	15.36	6.06	6.45	11.56

6.2. Measurement error analysis of the FMS-D, FMS-E, and FMS-F

6.2.1. Mean measurement error analysis of the FMS-D, FMS-E, and FMS-F

The mean measurement error rates of the FMS-D, FMS-E, and FMS-F in F_x, F_y, and M_z component are shown in Table 5. From this table, we know that the mean measurement error rates of the FMSs are mostly lower than 0.1 % when the shock loads are applied, lower than 0.6 % when the sine loads C are applied, and lower than 0.25 % when the sine loads D are applied. This result indicates that it is feasible to treat the mean elastic output after the inertia compensation as the static aerodynamic loads. In addition, the mean measurement errors are close to each other by comparing the output results of them under the same loading.

Table 5. Mean measurement error rates of the FMS-D, FMS-E, and FMS-F after the inertia compensation.

Load frequency	FMS-D			FMS-E			FMS-F		
	F_x (‰)	F_y (‰)	M_z (‰)	F_x (‰)	F_y (‰)	M_z (‰)	F_x (‰)	F_y (‰)	M_z (‰)
Shock loads	0.76	0.34	0.54	0.14	0.33	0.54	0.93	0.57	0.62
Sine loads C	2.27	5.59	0.84	1.61	0.81	0.78	1.32	0.52	0.88
Sine loads D	0.82	1.23	2.09	0.14	0.97	0.68	0.38	1.16	1.40

6.2.2. Transient measurement error analysis of the FMS-D, FMS-E, and FMS-F

The transient measurement errors of the FMS-D, FMS-E, and FMS-F are shown in Figure 18. Figure 18 (a) - (c) are the measurement errors of the FMS-D in each component, and (d) - (f) are the measurement errors of the FMS-E, and (g) - (i) are the measurement errors of the FMS-F.

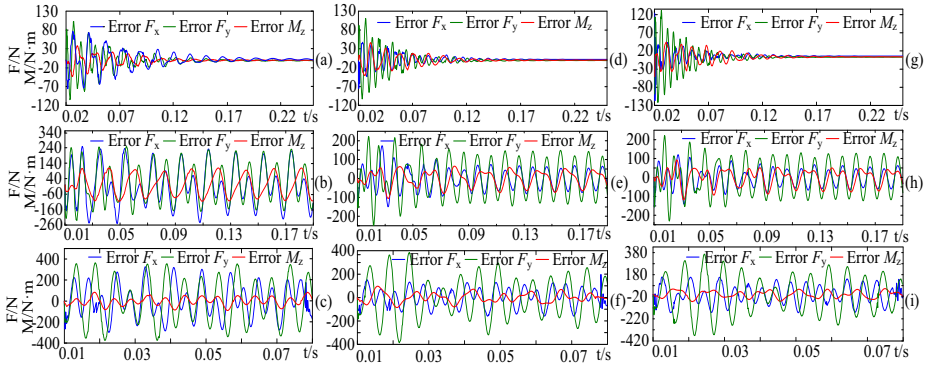

Figure 18. The transient measurement errors of FMSs, (a) - (c) the errors of FMS-D, (d) - (f) the errors of FMS-E, (g) - (i) the errors of FMS-F.

Table 6 shows the maximum transient measurement error rates of the FMS-D, FMS-E, and FMS-F after the inertia compensation. We can find in this table that the transient output histories of the FMSs are close to the input loads. Meanwhile, the measurement error of F_x decrease firstly, and then keep remained with the stiffness of the float frame. The measurement error of F_y keep remained firstly, and then increase with the stiffness of the float frame. The measurement error of M_z keep remained firstly, and then decrease with the stiffness of the float frame.

Table 6. The maximum measurement error rates of the FMS-D, FMS-E, and FMS-F after the inertia compensation.

Load	FMS-D (%)			FMS-E (%)			FMS-F (%)		
	Shock loads	Loads A	Loads B	Shock loads	Loads A	Loads B	Shock loads	Loads A	Loads B
F_x	5.18	12.55	16.36	3.75	8.69	7.96	3.74	7.82	8.27
F_y	3.52	8.28	12.51	3.69	8.30	12.87	4.13	11.57	14.43
M_z	4.39	10.98	9.01	4.67	10.60	9.77	3.94	5.93	6.40

7. Conclusions

In this paper, the transient simulations of the FMSs are carried out through the FEM to study the effect of force balance parameters to the output of the FMS. The following conclusions can be drawn.

1. It is feasible to treat the mean measurement result after the inertia compensation as the static aerodynamic load. The force balance stiffness and the float frame stiffness have a small influence on the mean measurement result.

2. On a certain range, the transient measurement error rate of F_x has a small relationship with the stiffness of the force balance, but transient measurement error rates of F_y and M_z decrease with increase of the force balance stiffness.

3. The transient measurement error rate of F_x decrease firstly, and then keep remained with the increase of balance float frame stiffness, the transient measurement error of F_y keep remained firstly, and then increase with increase of balance float frame stiffness, and the transient measurement error of M_z keep remained firstly, then decrease with increase of balance float frame stiffness.

References

[1] Stalker R J. A study of the free-piston shock tunnel. AIAA J., 1967, 5(5), 2160-2165.
[2] Pate S R, Silm L G, Stallings D W, Wagner D. Development of an MHD-Augmented, High Enthalpy, Shock Tunnel Facility. AIAA J., 1974, 12(3), 289-297, doi: 10.2514/3.49223.
[3] Olivier H, Groenig H, Bozec A L. Hypersonic model testing in a shock tunnel. AIAA J., 1995, 33(2), 262-265.
[4] Robinson M J, Mee D J, Tsai C Y, Bakos R J. Three-Component Force Measurements on a Large Scramjet in a Shock Tunnel. J. Spacecr. Rockets, 2004, 41(3), 416-425, doi: 10.2514/1.10699.
[5] Schultz I A, Goldenstein C S, Strand C L, Goyne C P. Hypersonic scramjet testing via diode laser absorption in a reflected shock tunnel. J. Propul. Power, 2014, 30(6), 1586-1594, doi: 10.2514/1.B35220.
[6] Tanno H, Kodera M, Komuro T, Sato K, Takahasi M, Itoh K M. Aerodynamic force measurement on a large-scale model in a short duration test facility. Rev. Sci. Instrum., 2005, 76(3), 035107, doi: 10.1063/1.1865815.
[7] Tanno H, Komuro T, Sato K, Itoh K. Aerodynamic force measurement technique with accelerometers in the impulsive facility HIEST. Shock Waves, 2009, 471-476, doi: 10.1007/978-3-540-85168-4_75.
[8] Tanno H, Komuro T, Takahashi M, Takayama K, Ojima H, Onaya S. Unsteady force measurement technique in shock tubes. Rev. Sci. Instrum., 2004, 75(2), 532-536, doi: 10.1063/1.1641156.
[9] Singh P, Menezes V, Irimpan K J, Hosseini H. Impulse force balance for ultrashort duration hypersonic test facilities. Shock and Vibration, 2015, 803253, 1-8, doi: 10.1063/1.1641156.
[10] Singh P, Trivedi S, Menezes V, Hosseini H. Dynamic Calibration and Validation of an Accelerometer Force Balance for Hypersonic Lifting Models. Sci. World J., 2014, 813759, 1-8, doi: 10.1155/2014/813759.
[11] Sahoo N, Suryavamshi K, Reddy K P, Mee D J. Dynamic force balances for short-duration hypersonic testing facilities. Exp. Fluids, 2005, 38(5), 606-614, doi: 10.1007/s00348-005-0932-5.

[12] Trivedi S, Menezes V. Measurement of yew, pitch and side force on a lifting model in a hypersonic shock tunnel. Measurement, 2012, 45, 1755-1764, doi: 10.1016/j.measurement.2012.04.008.
[13] Satheesh K, Jagadeesh G. Analysis of an internally mountable accelerometer balance system for use with non-isotropic models in shock tunnels. Measurement, 2009, 42, 856-862, doi: 10.2514/1.38914.
[14] Saravanan S, Jagadeesh G, Reddy K P J. Aerodynamic force measurement using 3-component accelerometer force balance system in a hypersonic shock tunnel. Shock Waves, 2009, 18(6), 425-435, doi: 10.1007/s00193-008-0172-8.
[15] Saravanan S, Jagadeesh G, Reddy K P. Aerodynamic force measurement using 3-component accelerometer force balance system in a hypersonic shock tunnel. Shock Waves, 2008, 18(6), 425-435, doi: 10.1007/s00193-008-0172-8.
[16] Naumann K W, Ende H, Mathieu G, George A. Millisecond aerodynamic force measurement with side-jet model in the ISL shock tunnel, AIAA J., 1993, 31(6), 1068-1074, doi: 10.2514/3.11730.
[17] Robinson M, Hannemann K. Short duration force measurements in impulse facilities, Proc., AIAA Aerodynamic Measurement Technology and Ground Testing Conference, 2006, AIAA San Francisco, California, doi: 10.2514/6.2006-3439.
[18] Smith A L, Mee D J, Daniel W J, Shimoda T. Design, modelling and analysis of a six component force balance for hypervelocity wind tunnel testing. Comput. Struct., 2001, 79(11), 1077-1088, doi: 10.1016/S0045-7949(01)00005-0.
[19] Laurence S, Hornung H G. Image-based force and moment measurement in hypersonic facilities. Exp. Fluids, 2008, 46(2), 343-353, doi: 10.1007/s00348-008-0565-6.
[20] Laurence S, Karl S. An improved visualization-based force-measurement technique for short-duration hypersonic facilities. Exp. Fluids, 2009, 48(6), 949-965, doi: 10.1007/s00348-009-0780-9.
[21] Pieterse F F, Bidgood P M. An experimental four-component optical fiber balance. Proc., 2015 AIAA Aerospace Sciences Meeting, AIAA, Kissimmee, Florida.
[22] Li S C, Liu Z H, Gao H L, et al. A New Airframe/Propulsion-Integrated Aerodynamic Testing Technology in Hypersonic Wind Tunnel. IEEE T Instrum Measurement, 2022, 71:1-9, doi: 10.11729/syltlx20180053.
[23] Li S C, You Z C, Gao H L, et al. Force measurement and support integrated device in hypersonic wind tunnel, IEEE T Instrum Measurement, 2022, 71:1-9.
[24] Collopy A X, Lee S, Marineau E C. Development of dynamic force measurement capabilities at AEDC Tunnel 9. Proc., 52rd AIAA Aerospace Sciences Meeting, AIAA, National Harbor, Maryland, doi: 10.2514/6.2014-0983.
[25] Marineau E C, MacLean M, Mundy E P, Holden M S. Force measurements in hyper-velocity flows with an acceleration compensated piezoelectric balance. J. Spacecr. Rockets, 2011, 48(4), 697-700.
[26] Watari M. Aerodynamic Force Extraction from Shock Tunnel Measurements Using the Oscillation Identification Technique. Trans. Japan Soc Aero. Space, 2007, 50(169), 169-174, doi: 10.2322/tjsass.50.169
[27] Shichao Li, Yi Sun, Hongli Gao, et al. An interpretable aerodynamic identification model for hypersonic wind tunnels, IEEE Transactions on Industrial Informatics, 2023, doi: 10.1109/LiTII.2023.3254644.
[28] Yi S, Li, Shichao, Gao H L. Transfer Learning: A New Load Identification Network Based on Adaptive Emd and Soft Thresholding in Hypersonic Wind Tunnel, Chinese Journal of Aeronautics, 2023, doi.org/10.1016/j.cja.2023.03.024.
[29] Wang Y, Liu Y, Luo C, Jiang Z. Force measurement using strain-gauge balance in a shock tunnel with long test duration. Rev. Sci. Instrum., 2016, 87(5), 1-8, doi: 10.1063/1.4950781.
[30] Li S C, Wang Y, Liu Y, Jiang Z. Design of a pulse-type strain gauge balance for a long-test-duration hypersonic shock tunnel. Shock Waves, 2016, 26, 835-44, doi: 10.1007/s00193-015-0616-x.
[31] Lv J Zh, Zhang X Q, Chen G X, Liu W X, Wang F. Transient research of force measuring balance to impulse combustion wind tunnel based on inertia compensation. Journal of vibration and shock, 2018, 37(2): 216-222. (in Chinese).
[32] Lv J Z, Zhang X Q, Chen G. X, Wu Y C. Transient dynamics research on the force-measurement system for hypersonic impulse combustion wind tunnel based on inertia compensation. J. Aerosp. Eng., 2018, 31(6): 04018094, doi: 10.1061/(asce)as.1943-5525.0000914.